Efficient solution method for the Reynolds equation with Herschel–Bulkley fluids

van der Meer, G. H.G.; van Ostayen, R. A.J.

DOI
10.1016/j.triboint.2024.110460

Publication date
2025

Document Version
Final published version

Published in
Tribology International

Tribology International 204 (2025) 110460

Contents lists available at ScienceDirect

Tribology International

journal homepage: www.elsevier.com/locate/triboint

Full Length Article

Efficient solution method for the Reynolds equation with Herschel–Bulkley fluids

G.H.G. van der Meer *, R.A.J. van Ostayen

Delft University of Technology, Department of Precision and Microsystems Engineering, Mekelweg 2, Delft, 2628 CD, The Netherlands

ARTICLE INFO

Keywords:
Generalised Reynolds equation
Non-Newtonian fluids
Journal bearing
Finite element method

ABSTRACT

Thin film lubrication problems frequently involve the use of lubricants with non-Newtonian characteristics, and a relatively simple viscosity model that can describe several non-Newtonian fluids is the Herschel–Bulkley relation. This relation can model solid-like properties of a lubricant at low shear stress using a yield stress, while at higher shear stress values shear-thinning or thickening can be included. In literature, this viscosity model has been combined with various governing equations to solve the non-Newtonian thin film problem, resulting in models that range from full 3D CFD simulations, to 1D Reynolds equation based methods. However, something that all of these approaches have in common is that they are either computationally expensive, can only be used for 1D geometries, or use non-exact, regularised versions of the Herschel–Bulkley model for reasons of numerical stability. This paper therefore introduces a method for solving a thin film problem with a non-regularised Herschel–Bulkley lubricant using the 2D generalised Reynolds equation, and this approach is shown to be fast without compromising on accuracy. The increased speed will allow the model to be used more efficiently in complex simulations or design optimisation scenarios.

1. Introduction

The increasing demands placed on bearing systems, such as stern tube bearings found in ships, require hydrodynamic bearings that can function at higher loads and with lower friction, for both lower and higher speeds. For these increasingly stringent goals to be met, fast and accurate numerical models that can for example be used in design optimisation studies, are essential. One aspect of a good model is a proper understanding of the behaviour of the lubricant, which is frequently assumed to be Newtonian. However, even more traditional oils and greases can display non-Newtonian behaviour [1,2], and these non-Newtonian effects are even more important when considering newer 'smart' lubricants, such as magnetorheological fluids [3]. It is clear that Newtonian models do not suffice in these cases, and non-Newtonian effects will have to be taken into account to obtain an accurate model.

In order to include the non-Newtonian effects of the lubricant, a viscosity model is needed which describes the relation between the shear stress and the shear rate of the lubricant. Many different empirical viscosity models for non-Newtonian fluids can be found in literature. Three of the simpler models, all with only 2 or 3 parameters, are the Bingham plastic model, the Ostwald–de Waele model or power law model, and the Herschel–Bulkley model. A Bingham plastic is a fluid with a yield stress, which means that the fluid is considered a solid when the internal stress is below the yield stress, and that the fluid behaves like a Newtonian fluid otherwise. The part of the fluid flow domain that behaves like a solid is also called the plug or the core. This Bingham plastic model is quite popular due to its simplicity, and has for example been used to model grease-lubricated bearings [4,5], as well as magneto- and electro-rheological lubricants [6,7]. An overview containing a large number of other applications from various fields has been created by Bird et al. [8]. In contrast to the Bingham plastic, a power law fluid does not have a yield stress, but is one of the simpler models that includes the effects of a shear-dependent viscosity. It has frequently been applied to model a wide variety of shear-thinning (pseudoplastic) and shear-thickening (dilatant) lubricants [9,10]. Finally, the Herschel–Bulkley model combines the Bingham plastic and power law characteristics and can therefore represent a fluid with both a yield stress and a shear-dependent viscosity. Depending on the lubricant, using this more general model can lead to a better match between simulations and experiments, but it will results in more complex numerical models that are less likely to converge [11–13].

Next to the viscosity model itself, a modelling approach is needed to combine the viscosity model with either the Reynolds equation or the Navier–Stokes equations. A number of different approaches can be found in literature to do this for bearing systems.

One approach is to derive modified Reynolds equations for the different cases of core formation of a Bingham plastic (i.e. a core sticking

* Corresponding author.
E-mail address: G.H.G.vanderMeer@tudelft.nl (G.H.G. van der Meer).

https://doi.org/10.1016/j.triboint.2024.110460
Received 25 October 2024; Received in revised form 4 December 2024; Accepted 8 December 2024
Available online 15 December 2024

List of Symbols

c_{AD}	Variable used for artificial diffusion
c_f	Cavitation transformation constant
D	Shaft diameter
f	Shear stress factor
F_n	Flow factor n
f_n	Component of flow factor n
g_n	Flow factor integral n
h	Film thickness
h_e	Mesh size
K	Consistency index
k_{AD}	Artificial diffusion coefficient
L	Bearing length
m	Flow index
n	Flow factor index ($n = 0, 1, 2$)
p	Film pressure
p_{cav}	Cavitation pressure
q	Flow rate
R	Shaft radius
T_τ	Dimensionless shear stress
u	Fluid speed
u_{AD}	Convection coefficient used for artificial diffusion
W	Load capacity
x	streamline direction
y	crosswind direction
z	thickness direction
z_m	z-coordinate of minimum shear
$\vec{\nabla}$	Gradient operator $\left[\frac{\partial}{\partial x}, \frac{\partial}{\partial y}\right]$

Greek symbols

ε	Eccentricity
η	Apparent viscosity
ξ	Variable combining p and ψ
τ	Shear stress
τ_c	Constant part of shear stress
τ_m	Minimum shear stress
τ_p	Lower bound of flow factor integrals
τ_{yld}	Yield stress
ϕ	Attitude angle
ψ	Lubricant fraction
ω	Radial velocity

Subscripts

v_0	Reference value for variable v
v_a	Variable v on the lower surface ($z = 0$)
v_b	Variable v on the upper surface ($z = 1$)
v_x	The x component of vector $\vec{v}$

Superscripts

$\bar{v}$	Indicates a variable with dimensions
$\vec{v}$	Indicates a vector with x and y components

Appell F1 function

α	1st argument
β	2nd argument
β'	3rd argument
γ	4th argument
x'	5th argument
y'	6th argument
w	Integration variable

to one of the bearing surfaces, a floating core, or no core formation at all). This was first done by Wada et al. who derived implicit 2D Reynolds equations for a Bingham plastic, that they applied to a step bearing and a journal bearing [14–16]. Later on, Tichy managed to derive explicit Reynolds equations for the different core cases of a 1D Bingham plastic flow [17]. The disadvantage of these methods is that it can be difficult to find explicit Reynolds equations for all cases of core formation, especially in 2D flows. The advantage is that once the equations have been found, convergence is fast.

Another approach that is commonly used is based on the generalised Reynolds equation introduced by Dowson [18]. Because this more general variant of the standard Reynolds equation allows for viscosity variations over the height of the lubricant film, it can be used to properly account for non-Newtonian effects. An oft-cited paper that implements this method in 2D for a Bingham plastic was published by Dorier and Tichy [19]. By using the generalised Reynolds equation they did not have to define separate equations for the different core cases, however, they did have to implement a regularisation of the Bingham plastic model to prevent convergence issues due to the discontinuity in the viscosity caused by the yield stress. Many similar publications, also ones using power law models and regularised variants of the Herschel–Bulkley relation, can be found in literature [11,20–24]. It should be noted that while this approach does not require multiple equations for the different core cases, a (slightly) modified version of the original problem is being solved in case a yield stress is used, because of the regularisation that has to be applied to those viscosity models. It is also known that regularisation of yield stress viscosity models can lead to incorrect predictions for the location of the core [25]. Furthermore, the solution process is computationally expensive for this approach, due to several integral terms in the generalised Reynolds equation that are evaluated numerically in most papers. Lampaert and van Ostayen found analytical solutions for these integrals in the case of a Bingham plastic, drastically reducing the required computation time [26]. By tracking the location of the core they also managed to circumvent the need for regularisation, while still only having one equation for all cases of core formation.

A final approach of including non-Newtonian effects in lubrication problems is to use CFD, solving the full 3D Navier–Stokes equations. This has been done by several researchers for various viscosity models, and generally gives good results [27–29]. The obvious disadvantage is that this method requires solving the Navier–Stokes equations, which is very computationally expensive.

In summary, there is quite a large body of research on the inclusion of non-Newtonian effects in the modelling of lubricating films. However, as far as the authors have been able to find, there is a lack of fast, 2D Reynolds equation based implementations using non-regularised viscosity models (other than Bingham plastic). The goal of this paper is therefore to show that it is possible to speed up the solution process of the generalised Reynolds equation in combination with an exact, non-regularised Herschel–Bulkley viscosity model, following a method similar to the one employed by Lampaert and van Ostayen [26]. To make the resulting model more relevant to real world (journal) bearings, mass-conserving cavitation will be taken into account as well.

2. Method

In this paper, the generalised Reynolds equation introduced by Dowson [18] is used as the basis for modelling a laminar thin film flow of a Herschel–Bulkley fluid. The method section will first introduce

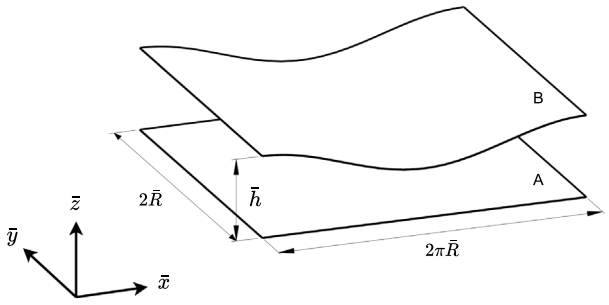

Fig. 1. Schematic overview of the problem geometry, in this case for a journal bearing. The two surfaces are marked as A and B.

the characteristics of these specific non-Newtonian fluids, followed by a derivation of the generalised Reynolds equation. Next, a more efficient way of solving this equation in combination with a Herschel–Bulkley fluid is derived. Finally, the numerical implementation in COMSOL Multiphysics® [30] will be discussed and validated.

The bearing geometry that will be analysed in this paper is shown in Fig. 1.

2.1. Herschel–Bulkley viscosity model

The governing equations and boundary conditions in this paper are made dimensionless using the groups below. The quantities with a bar (e.g. $\bar{x}$) have dimensions, the quantities without bar are dimensionless. Note that similar notation is used for 2D vectors with an x and y component, which are indicated with an arrow (e.g. $\vec{\tau}$).

$$x = \frac{\bar{x}}{\bar{R}},\quad y = \frac{\bar{y}}{\bar{R}},\quad z = \frac{\bar{z}}{h\bar{h}_0},\quad h = \frac{\bar{h}}{\bar{h}_0},\quad \eta = \frac{\bar{\eta}}{\bar{\eta}_0},\quad u = \frac{\bar{u}}{\bar{u}_0},$$

$$p = \frac{\bar{h}_0^2}{\bar{\eta}_0\bar{u}_0\bar{R}}\bar{p},\quad \tau = \frac{\bar{h}_0}{\bar{\eta}_0\bar{u}_0}\bar{\tau} = T_\tau\bar{\tau},\quad q = \frac{1}{\bar{h}_0\bar{u}_0}\bar{q}$$

Here x and y denote the in-plane coordinates, z the coordinate normal to the lubrication film, h the local film height, η the viscosity, u the fluid velocity, p the pressure, τ the shear stress, and q the flow rate. The z-coordinate is defined to be between 0 (for lower surface a) and 1 (for upper surface b). These quantities were made dimensionless using several constants, where $\bar{R}$ is the shaft radius, $\bar{h}_0$ the nominal film thickness, and $\bar{\eta}_0$ and $\bar{u}_0$ are reference values for the viscosity and velocity respectively.

The Herschel–Bulkley model is a non-Newtonian viscosity model that describes a fluid that has a yield stress and is either shear-thinning or shear-thickening for shear stresses above this critical yield stress. For this model the relation between the shear stress $\vec{\bar{\tau}}$ and the velocity gradient (the shear rate) $\partial\vec{\bar{u}}/\partial\bar{z}$ is described by Eq. (1), with the three parameters being the yield stress $\bar{\tau}_{yld}$, the consistency index $\bar{K}$, and the flow index m. When the shear stress is lower than the yield stress ($|\vec{\bar{\tau}}| < \bar{\tau}_{yld}$) the fluid is considered to be solid, and shear stress larger than the yield stress leads to viscous flow. The type of viscous flow is determined by the flow index, with the fluid showing pseudoplastic (shear-thinning) behaviour for $m < 1$, and dilatant (shear-thickening) behaviour for $m > 1$.

For $\bar{\tau}_{yld} \neq 0$ and $m = 1$ the Herschel–Bulkley model reduces to the Bingham plastic model. For $\bar{\tau}_{yld} = 0$ and $m \neq 0$ the model reduces to a power law model. Finally, when both $\bar{\tau}_{yld} = 0$ and $m = 1$, the model reduces to the Newtonian model.

$$|\vec{\bar{\tau}}| = \bar{\tau}_{yld} + \bar{K}\left|\frac{\partial\vec{\bar{u}}}{\partial\bar{z}}\right|^m \tag{1}$$

The Herschel–Bulkley model can be rewritten using Eq. (2), where both the shear stress factor f (Eq. (3)) and the apparent viscosity η (Eq. (4)) will be given as functions of the shear stress magnitude. This will prove useful later on in the derivation. The equations are made dimensionless at the same time.

$$f\vec{\tau} = \frac{\eta}{h}\frac{\partial\vec{u}}{\partial z} \tag{2}$$

$$f = \left(1 - \frac{\tau_{yld}}{|\vec{\tau}|}\right)^{\frac{1}{m}} f^*\left(|\vec{\tau}|\right)$$
$$f^*\left(|\vec{\tau}|\right) = \begin{cases} 1 & \text{if} \quad |\vec{\tau}| \geq \tau_{yld} \\ 0 & \text{if} \quad |\vec{\tau}| < \tau_{yld} \end{cases} \tag{3}$$

$$\eta = \frac{\bar{K}^{\frac{1}{m}}}{\bar{\eta}_0}\left|\frac{\vec{\tau}}{T_\tau}\right|^{1-\frac{1}{m}} \tag{4}$$

2.2. Generalised Reynolds equation

This section presents the derivation of a generalised Reynolds equation that can be used to solve non-Newtonian lubrication problems. Following the derivation of Dowson [18], the linear momentum equation for a laminar thin film flow with negligible body and inertial forces is given by Eq. (5). In this equation $\vec{p}$ is the pressure, $\vec{\tau}$ is the shear stress, and $\vec{\nabla} = [\partial/\partial x, \partial/\partial y]$ is the gradient operator. Note that the dimensionless film thickness h appears only due to the non-dimensionalisation chosen in this paper.

$$\vec{\nabla}p = \frac{1}{h}\frac{\partial\vec{\tau}}{\partial z} \tag{5}$$

Integrating once over the film thickness coordinate z leads to an expression for the shear stress $\vec{\tau}$ (Eq. (6)), with $\vec{\tau}_c$ the as of yet unknown integration constant.

$$\vec{\tau} = zh\vec{\nabla}p + \vec{\tau}_c \tag{6}$$

The next step is to substitute for $\vec{\tau}$ in this equation using Eq. (2), and to integrate over z again. Combined with the standard no-slip boundary conditions for the flow velocity ($\vec{u} = \vec{u}_a$ at $z = 0$ and $\vec{u} = \vec{u}_b$ at $z = 1$), this leads to Eqs. (7) and (8) which represent the flow velocity $\vec{u}$ and the constant part of the shear stress $\vec{\tau}_c$ respectively ($\vec{\tau}_c$ is also the shear stress at $z = 0$). Note that it should also be possible to include slip boundary conditions without fundamentally changing the derivation that follows. For this, the reader is referred to [31], where Navier slip is added to the generalised Reynolds equation.

$$\vec{u} = h^2\vec{\nabla}p\int_0^z \frac{f}{\eta}z\mathrm{d}z + h\vec{\tau}_c\int_0^z \frac{f}{\eta}\mathrm{d}z + \vec{u}_a \tag{7}$$

$$\vec{\tau}_c = \frac{\vec{u}_b - \vec{u}_a}{hF_0} - h\frac{F_1}{F_0}\vec{\nabla}p \tag{8}$$

The flow factor integrals F_0 and F_1 that appear in Eq. (8) are defined by Eq. (9), where n can be either 0, 1 for F_0 and F_1, or 2 for F_2 which is used in the relations that follow.

$$F_n = \int_0^1 \frac{f}{\eta}z^n\mathrm{d}z \tag{9}$$

The flow rate through a cross-section of the film $\vec{q}$ can be obtained by integrating the flow velocity $\vec{u}$ over the channel height. Using integration by parts and substituting for $\vec{\tau}_c$ results in Eq. (10).

$$\vec{q} = -h^3\left(F_2 - \frac{F_1^2}{F_0}\right)\vec{\nabla}p + h\left(1 - \frac{F_1}{F_0}\right)\vec{u}_b + h\frac{F_1}{F_0}\vec{u}_a \tag{10}$$

Finally, substituting for $\vec{q}$ in the mass balance equation (Eq. (11)) will result in the generalised Reynolds equation. Here ψ is the lubricant fraction that is used to take cavitation into account.

$$\vec{\nabla}\left(\psi\vec{q}\right) = 0 \tag{11}$$

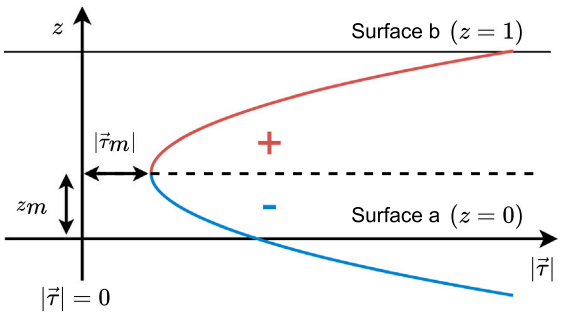

Fig. 2. A schematic representation of the shear stress magnitude $|\vec{\tau}|$ over the film height. The minimum shear stress $|\vec{\tau}_m|$ and the z-coordinate of the minimum shear stress z_m are indicated. The red part of $|\vec{\tau}|$ (above $z = z_m$) corresponds to the positive solutions of Eq. (20), the blue part (below $z = z_m$) corresponds to the negative solutions.

2.2.1. Cavitation algorithm

In this paper, cavitation is modelled using the mass-conservative JFO boundary conditions [32]. These boundary conditions are implemented with a variable transformation that is used to replace both p and ψ with functions of a new variable ξ (Eqs. (12) & (13)). By assuming that at any point in the fluid film, the lubricant is either in a full film region ($p > 0$, $\psi = 1$) or in a cavitated region ($p = 0$, $0 \leq \psi < 1$), the Reynolds equation can be solved for a single variable ξ that represents either the pressure or the lubricant fraction, depending on its sign.

$$p = (\xi \geq 0)\xi \tag{12}$$

$$\psi = 1 + (\xi < 0)c_f \xi \tag{13}$$

A numerical stabilisation technique is required to properly solve the generalised Reynolds equation in combination with this cavitation algorithm. For that reason artificial diffusion will be used in both the streamline and crosswind directions (x and y). The amount of cavitation can be controlled with the transformation constant c_f. The Appendix discusses the implementation of the numerical stabilisation algorithm, as well as an optimal value for c_f, resulting in Eq. (14) when assuming isotropic diffusion.

$$\vec{\nabla}\left(-h^3\left(F_2 - \frac{F_1^2}{F_0}\right)\vec{\nabla}\xi + \psi h\left(1 - \frac{F_1}{F_0}\right)\vec{u}_b + \psi h \frac{F_1}{F_0}\vec{u}_a\right) = 0 \tag{14}$$

2.3. Analytical evaluation of flow factors integrals

The generalised Reynolds equation (Eq. (11)) is sufficient to determine the pressure profile for a thin film flow of a non-Newtonian lubricant. This equation has to be solved together with the flow factor integrals (Eq. (9)), since these integrals depend on the shear stress and therefore on the pressure gradient. As was discussed in the introduction, this calculation has been performed previously for various viscosity models, both with and without cavitation. However, in almost all of these papers the calculation of the flow factor integrals seems to be performed using numerical integration, and an analytical solution has only been found for Bingham fluids [26]. Since these integrals have to be evaluated at every single point in the domain, for every iteration of the solver, this is a fairly computationally expensive part of the calculation. In this section it will be shown that it is also possible to analytically evaluate the three flow factor integrals F_0, F_1 and F_2 for a Herschel–Bulkley fluid, removing the need for slow numerical integration.

In order to analytically evaluate the flow factor integrals, they have to be written to a different form. Currently these integrals, as given by Eq. (9), are integrated over the film thickness coordinate z. For the analytical evaluation it is necessary to rewrite them such that the integration is performed over the shear stress $|\vec{\tau}|$. This is done in Eq. (15), where $|\vec{\tau}_b|$ and $|\vec{\tau}_a|$ are the shear stress magnitudes on the upper and lower surfaces respectively.

$$F_n = \int_{|\vec{\tau}_a|}^{|\vec{\tau}_b|} \frac{f}{\eta} z^n \frac{\partial z}{\partial |\vec{\tau}|} \mathrm{d}|\vec{\tau}| \tag{15}$$

Evaluating Eq. (15) requires z as a function of $|\vec{\tau}|$, as well as the partial derivative $\partial z/\partial \tau$. To find these quantities, the shear stress magnitude should be determined first. This can be done using Eq. (6), and results in Eq. (16).

$$|\vec{\tau}|^2 = z^2 h^2 |\vec{\nabla} p|^2 + 2zh(\vec{\nabla} p \cdot \vec{\tau}_c) + |\vec{\tau}_c|^2 \tag{16}$$

With the (square of the) shear stress magnitude known, the z-coordinate of the minimum shear stress z_m can be determined (Eq. (17)), as well as the minimum shear stress magnitude $|\vec{\tau}_m|$ (Eq. (18)). See Fig. 2 for a visual representation of the shear stress magnitude and the minimum shear stress. Note that this transformation is ill-defined when $|\vec{\nabla} p| \to 0$, which is the case (most notably) in the cavitation region. This case will be treated at the end of this section.

$$z_m = -\frac{\vec{\nabla} p \cdot \vec{\tau}_c}{h|\vec{\nabla} p|^2} \tag{17}$$

$$|\vec{\tau}_m|^2 = |\vec{\tau}_c|^2 - \frac{(\vec{\nabla} p \cdot \vec{\tau}_c)^2}{|\vec{\nabla} p|^2} \tag{18}$$

Eq. (16) for the shear stress magnitude can now be rewritten using Eqs. (17) and (18), resulting in Eq. (19).

$$|\vec{\tau}|^2 = |\vec{\tau}_m|^2 + h^2 (z - z_m)^2 |\vec{\nabla} p|^2 \tag{19}$$

Rewriting Eq. (19) then leads to z as a function of $|\vec{\tau}|$, which can be used to calculate the partial derivative $\partial z/\partial|\vec{\tau}|$ (Eqs. (20) and (21) respectively). Because the shear stress magnitude is symmetric around the minimum shear stress, both equations have two solutions.

$$z = z_m \pm \frac{1}{h|\vec{\nabla} p|}\left(|\vec{\tau}|^2 - |\vec{\tau}_m|^2\right)^{1/2} \tag{20}$$

$$\frac{\partial z}{\partial |\vec{\tau}|} = \pm \frac{1}{h|\vec{\nabla} p|} \frac{|\vec{\tau}|}{\left(|\vec{\tau}|^2 - |\vec{\tau}_m|^2\right)^{1/2}} \tag{21}$$

Eqs. (20) and (21) can now be substituted into the flow factor integrals (Eq. (15)). However, z and its derivative are both multivalued functions of $|\vec{\tau}|$, which means that these functions have two solutions for every value of $|\vec{\tau}|$. As a results, the bounds of the integral in Eq. (15) are not uniquely defined and the integral cannot be evaluated directly. The following paragraphs describe how to modify the integral such that it can be evaluated.

Since the shear stress magnitude has a minimum (Eqs. (16) through (19)), it is known that $|\vec{\tau}_m| \leq |\vec{\tau}| < \infty$. Therefore, instead of integrating directly from $|\vec{\tau}_a|$ to $|\vec{\tau}_b|$ as in Eq. (15), it is better to split the integral at $|\vec{\tau}_m|$, resulting in Eq. (22).

$$F_n = \int_{|\vec{\tau}_m|}^{|\vec{\tau}_b|} \frac{f}{\eta} z^n \frac{\partial z}{\partial |\vec{\tau}|} \mathrm{d}|\vec{\tau}| - \int_{|\vec{\tau}_m|}^{|\vec{\tau}_a|} \frac{f}{\eta} z^n \frac{\partial z}{\partial |\vec{\tau}|} \mathrm{d}|\vec{\tau}| \tag{22}$$

Looking at Eq. (20) with the knowledge that $|\vec{\tau}_m| \leq |\vec{\tau}| < \infty$, it is clear that the positive solutions corresponds to $z_m \leq z < \infty$, and the negative solutions to $-\infty < z \leq z_m$. This means that for the integrals in Eq. (22), the sign of z and $\partial z/\partial|\vec{\tau}|$ depends only on the z-coordinate of the surface represented by the upper bound of the integrals. Taking the situation in Fig. 2 as an example, here upper surface b lies above z_m, meaning that the first integral in Eq. (22) requires the positive solutions of z and $\partial z/\partial|\vec{\tau}|$. Meanwhile, the second integral requires the negative solutions, since lower surface a lies below z_m.

For this reason, Eq. (22) can be rewritten to Eqs. (23) through (27). Eq. (26) shows that the $\pm$ signs from Eqs. (20) and (21) have

been replaced with the sgn function, which is equal to 1 for a positive argument, and −1 for a negative argument.

$$F_0 = f_0 \tag{23}$$

$$F_1 = f_1 + z_m f_0 \tag{24}$$

$$F_2 = f_2 + 2z_m f_1 + z_m^2 f_0 \tag{25}$$

$$f_n = \left(\frac{1}{h\left|\vec{\nabla}p\right|}\right)^{n+1} \left(\operatorname{sgn}(1-z_m)^{n+1} g_n\left(\left|\vec{\tau}_b\right|\right) - \operatorname{sgn}(0-z_m)^{n+1} g_n\left(\left|\vec{\tau}_a\right|\right)\right) \tag{26}$$

$$g_n(\tau) = \int_{|\vec{\tau}_m|}^{\tau} \frac{f}{\eta} |\vec{\tau}| \left(|\vec{\tau}|^2 - |\vec{\tau}_m|^2\right)^{\frac{n-1}{2}} \mathrm{d}|\vec{\tau}| \tag{27}$$

One final step that is necessary for the analytical evaluation of the flow factor integrals given by Eq. (27) concerns the lower bound of the integrals, $|\vec{\tau}_m|$. Since a Herschel–Bulkley fluid has a yield stress, it is possible for the minimum shear stress to be lower than the yield stress ($|\vec{\tau}_m| < \tau_{yld}$). However, for the analytical evaluation to be possible, the assumption has to be made that both bounds of the integral are larger than τ_{yld}. To ensure this, and knowing that $f = 0$ for any $|\vec{\tau}| < \tau_{yld}$ (Eq. (3)), the lower bound of Eq. (27) will be replaced by $|\vec{\tau}_p|$ which is defined by Eq. (28).

$$\left|\vec{\tau}_p\right| = \begin{cases} |\vec{\tau}_m| & \text{if} \quad |\vec{\tau}_m| \geq \tau_{yld} \\ \tau_{yld} & \text{if} \quad |\vec{\tau}_m| < \tau_{yld} \end{cases} \tag{28}$$

Using Eq. (28) and substituting for f and η (from Eqs. (3) and (4) respectively), Eqs. (26) and (27) can now be changed to Eqs. (29) and (30).

$$f_n = \frac{T_\tau \bar{\eta}_0}{(\bar{K}T_\tau)^{\frac{1}{m}}} \left(\frac{1}{h|\vec{\nabla}\vec{p}|}\right)^{n+1} \left(\operatorname{sgn}(1-z_m)^{n+1} g_n\left(\left|\vec{\tau}_b\right|\right) - \operatorname{sgn}(-z_m)^{n+1} g_n\left(\left|\vec{\tau}_a\right|\right)\right) \tag{29}$$

$$g_n(\tau) = \int_{|\vec{\tau}_p|}^{\tau} \left(|\vec{\tau}| - \tau_{yld}\right)^{\frac{1}{m}} \left(|\vec{\tau}|^2 - |\vec{\tau}_m|^2\right)^{\frac{n-1}{2}} f^*(\tau)\ \mathrm{d}|\vec{\tau}| \tag{30}$$

Note that Eq. (30) contains the f^* term from Eq. (3). As a results, if either $|\vec{\tau}_a|$ or $|\vec{\tau}_b|$ is smaller than the yield stress τ_{yld}, the corresponding integral $g_n(\tau)$ will be equal to zero. In a real bearing this would be the situation where the solid part of the fluid adheres to the surface where the shear stress is lowest.

The integral given by Eq. (30) has been integrated analytically using a software package for symbolic mathematical computation [33]. The indefinite variant of Eq. (29) was evaluated for $n = 0$, 1 and 2, resulting in Eqs. (31), (32) and (33) respectively.

$$g_0(\tau) = \left[\frac{\left(|\vec{\tau}|-\tau_{yld}\right)^{1+\frac{1}{m}}}{1+\frac{1}{m}} \left(\frac{1}{\tau_{yld}^2 - |\vec{\tau}_m|^2}\right)^{\frac{1}{2}} \operatorname{AppellF1}\left(1+\frac{1}{m}, \frac{1}{2}, \frac{1}{2}, 2+\frac{1}{m}, x', y'\right)\right]\Bigg|_{|\vec{\tau}_p|}^{\tau} \tag{31}$$

$$g_1(\tau) = \left.\frac{\left(|\vec{\tau}| - \tau_{yld}\right)^{1+\frac{1}{m}}}{1+\frac{1}{m}}\right|_{|\vec{\tau}_p|}^{\tau} \tag{32}$$

$$g_2(\tau) = \left[\frac{\left(|\vec{\tau}|-\tau_{yld}\right)^{1+\frac{1}{m}}}{1+\frac{1}{m}} \left(\frac{1}{\tau_{yld}^2 - |\vec{\tau}_m|^2}\right)^{-\frac{1}{2}} \operatorname{AppellF1}\left(1+\frac{1}{m}, -\frac{1}{2}, -\frac{1}{2}, 2+\frac{1}{m}, x', y'\right)\right]\Bigg|_{|\vec{\tau}_p|}^{\tau} \tag{33}$$

$$x' = \frac{-|\vec{\tau}| + \tau_{yld}}{|\vec{\tau}_m| + \tau_{yld}} \qquad y' = \frac{|\vec{\tau}| - \tau_{yld}}{|\vec{\tau}_m| - \tau_{yld}} \tag{34}$$

These analytical evaluations of the integrals are valid considering the following assumptions:

1. $\tau_{yld} \geq 0$
2. $|\vec{\tau}_m| \geq 0$
3. $|\vec{\tau}| \geq \tau_{yld}$
4. $|\vec{\tau}| \geq |\vec{\tau}_m|$

Finally, before continuing with the analysis of the resulting equations, it should be noted that the analytical evaluation of the flow factor integrals is not possible in the limit where $|\vec{\nabla}p| \to 0$. However, it is not necessary either, since in this case the shear stress is constant ($|\vec{\tau}| = |\vec{\tau}_c|$, see Eq. (16)), which means f and η are constant as well and can be moved outside of the integral in Eq. (9). The integral then becomes trivial to solve, resulting in Eq. (35), which can be used to calculate the flow factors in the cavitation region.

$$F_n = \frac{1}{n} \frac{f(|\vec{\tau}_c|)}{\eta(|\vec{\tau}_c|)} \quad \text{if} \quad |\vec{\nabla}p| = 0 \tag{35}$$

2.3.1. Appell F1 function

It turns out that while the analytical evaluation for g_1 is trivial, the evaluations for g_0 and g_2 are more complicated. These depend on the Appell hypergeometric function of the first kind, AppellF1 $(\alpha, \beta, \beta', \gamma, x', y')$, which is well-defined by an infinite series [34]. In literature, Appell functions have for example been found in the solution of integrals appearing in Feynman diagrams from quantum mechanics [35], and in the Watson integrals that characterise lattice random walks in biology [36].

Implementing the Appell F1 function using the infinite series is a complex procedure, since the series is only convergent for $|x'| < 1$ and $|y'| < 1$. Additional mathematical analysis is required to evaluate this series for other values of x' and y', and only one example of such an implementation could be found in literature [37]. An alternative method has been used in this paper, which solves a simple integral representation [38,39] of the Appell function (36). In this equation Γ is the standard gamma function.

$$\operatorname{AppellF1}(\alpha, \beta, \beta', \gamma, x', y') = \frac{\Gamma(\gamma)}{\Gamma(\alpha)\Gamma(\gamma-\alpha)} \int_0^1 w^{\alpha-1} w^{\gamma-\alpha-1} (1-wx')^{-\beta} (1-wy')^{-\beta'} \mathrm{d}w \tag{36}$$

This integral is valid as long as the conditions below are satisfied, which is the case for all positive values of the flow index m (see Eqs. (31) and (33)).

1. $\Re(\alpha) > 0$
2. $\Re(\gamma - \alpha) > 0$

A disadvantage of the integral representation is that numerical integration will be required to solve the Appell function. The analytical evaluation of the flow factor integrals is therefore no longer fully analytical, seemingly defeating its purpose. However, the Appell function is a known and well-defined mathematical function (in contrast to the flow factor integrals themselves). The use of the integral representation and numerical integration to calculate it, is therefore purely a limitation imposed by the poor availability of faster Appell function implementations based on the infinite series.

In order to show the potential of the analytical evaluation of the flow factor integrals in combination with a fast Appell function, lookup table approximations of the function were created. Two Appell function

lookup tables are required, one for Eq. (31) where $\beta = \beta' = 0.5$, and one for Eq. (33) where $\beta = \beta' = -0.5$. For the creation of these lookup tables, the flow index m was assumed to be constant (different values of m will therefore require the lookup tables to be recalculated). The remaining arguments, x' and y', can vary between $-\infty < x' \leq 1$ and $-\infty < y' < \infty$ respectively (see Eq. (34)). For the lookup tables the range of these variables will be limited to $-1e{-}4 < x' \leq 1$ and $-1e{-}4 < y' < 1e{-}4$, which was found to be sufficient for the simulations carried out in this paper (Eq. (36) will be solved numerically at runtime for values of x' and y' outside of this range). The tables contain 240 by 480 values (for x' and y' respectively), which logarithmically approach the singular point (1,1) to within 1e−6. Cubic spline interpolation is used to find values that are not contained in the table. Finally, this results in two 2D lookup tables of x' and y' which are both valid for a single value of m. Accessing these tables takes a fraction of the time that is required for numerical integration, and will therefore allow for fast solutions to the generalised Reynolds equation.

2.4. Software implementation

The system of equations that describe a Herschel–Bulkley lubrication film are solved using the commercial FEM software package COMSOL Multiphysics® 6.1 [30]. Two variants of this model are solved in this paper. Both variants solve the generalised Reynolds equation (Eq. (14)) for the pressure p, this equation is implemented in COMSOL using a General Form PDE. In addition, the first variant, the numerical variant, solves Eq. (9) for the flow factor integrals F_0, F_1 and F_2. The integrals are evaluated using COMSOL's numerical integration routine `integrate`. The second variant, the analytical variant, instead solves Eq. (9) together with Eqs. (23) through (25) for F_0, F_1 and F_2. In this case the integral is evaluated analytically, and the resulting Appell functions are evaluated using lookup tables (see Section 2.3.1). In both cases Dirichlet boundary conditions are used to set the pressure on the outer edges of the computational domain to zero. Furthermore, the symmetry of the bearing along the midline ($y = 0.5$) is used to find the pressure for only one half of the bearing.

The same solver strategy with two steps is used for both variants. In both cases, Eq. (14) is solved in step 1 for a Newtonian fluid, with $F_0 = 1$, $F_1 = 1/2$ and $F_2 = 1/3$. This Newtonian solution is then used as an initial guess for the Herschel–Bulkley solver in step 2, which solves for both the generalised Reynolds equation and the flow factor integrals at the same time. The flow factor integral derivatives are not included in the Jacobian matrix,[1] which was found to result in much better convergence. The solver therefore simply uses the flow factor function values from the previous step. A Newton–Raphson solver with under-relaxation is used for both steps, in step 1 the relaxation factor is determined automatically by COMSOL, in step 2 it is kept constant at a value of 0.2. Convergence is assumed when the relative solution and residual errors are smaller than 1e−3. The computational domain is discretised with a structured quadrilateral mesh, and unless mentioned otherwise the edge length of the elements is set equal to $h_e = 0.01$ (100×50 elements), which was found to be sufficient in mesh convergence checks using decreasing element size. Quadratic Lagrange shape functions are used.

The Appell function that is required for the analytical variant is calculated by solving Eq. (36) using the `integral` function of MATLAB [40]. The script that performs this calculation is based on an existing user-submitted implementation [41], and can be found at [42]. The lookup tables of the Appell function are made using the `griddedInterpolant` function in MATLAB. The resulting tables are created separately, before the model is solved, and are saved as .mat files. When the model is solved with COMSOL, the 'LiveLink for MATLAB' functionality can be used to call a MATLAB script that loads the lookup tables and returns the requested values of the Appell function.

[1] In COMSOL this can be achieved with the `nojac` operator.

Table 1
Overview of the two sets of operating conditions used for the validation of the model, as well as the conditions for the test case used to compare the numerical and analytical variants of the model.

	Fig. 3	Fig. 4	Test case	Unit
$\bar{D}$	100	50	50	mm
L/D	4/3	1	1	–
$\bar{h}_0$	145.5	235	100	μm
$\bar{K}$ & $\bar{\eta}_0$	0.0127	–	0.1	Pa s
τ_{yld}	0	0.8	0.25	–
m	1	1	1.2	–
$\bar{\omega}$	48.1	–	26.2	rad/s
ϵ	0.61	0.31 - 0.71	0.3 - 0.7	–
ϕ	0	0	$\pi/4$	–
$\bar{p}_{cav}$	72 139.79	–	101 325	Pa

2.5. Model validation

To validate the correct implementation of the equations, the numerical variant of the model will be compared with results found in literature for hydrodynamic journal bearings. No papers discussing the use of the isothermal Reynolds equation with a Herschel–Bulkley fluid model have been found, neither with nor without cavitation. For that reason the cavitation and non-Newtonian aspects of the model will be validated separately. In both cases the dimensionless film thickness h will be given by Eq. (37), where ϵ is the eccentricity of the shaft and ϕ the attitude angle.

$$h = 1 + \epsilon \cos(x - \phi) \tag{37}$$

Fig. 3 shows the pressure profile near the centreline of a journal bearing lubricated with a Newtonian lubricant, the operating conditions are shown in Table 1. The model result is compared with the numerical result of Brewe [43] (who modelled cavitation using Elrod's algorithm [44]) and the experimental result of Jakobssen and Floberg [45]. The pressure profile determined by the numerical variant of the model shows good agreement with both results, and was found to be mesh convergent.

The second validation was performed for a journal bearing lubricated with a Bingham fluid, which is identical to a Herschel–Bulkley fluid with the flow index m equal to 1. The pressure profiles calculated by the numerical variant of the model for several eccentricities are shown in Fig. 4, the operating conditions can be found in Table 1. For comparison, the numerical results obtained by Wada et al. and Gertzos et al. are shown [14,28]. They implemented cavitation using the half-Sommerfeld condition, for that reason the cavitation implementation of the model was disabled and the pressure profiles are only shown for the full film region of the bearing ($0 \leq x \leq 0.5$). Agreement between the model and the results from literature is good, and the model was once again found to be mesh convergent.

3. Results and discussion

To show that the analytical variant of the model gives the same results as the numerical variant, but does so much faster, both models will be applied to the same test case. The operating conditions for this test case can be found in Table 1, the test case describes a journal bearing at several different eccentricities lubricated with a Herschel–Bulkley fluid. The film thickness is once again given by Eq. (37). Fig. 5 shows the resulting pressure profiles at the midline of the bearing for five different eccentricity values, and Fig. 6 shows the full 2D pressure profile for one of these eccentricities. The differences between the results of the numerical and analytical variants of the model are very small, and cannot be distinguished using Fig. 5. For that reason the figure shows only the pressure profiles of one model variant, and the relative differences between the two variants are shown in Table 2 for the peak pressure and load capacity, with the load capacity W being determined using Eq. (38).

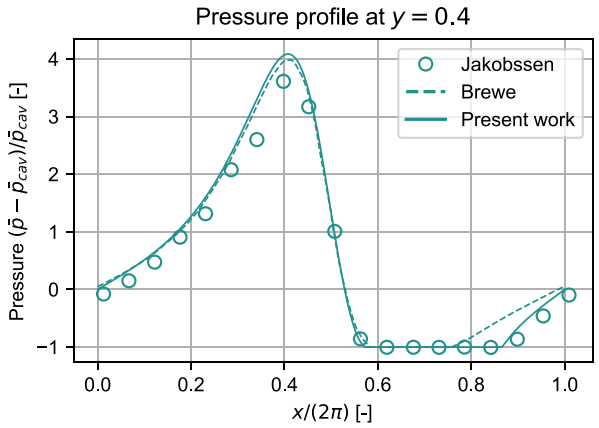

Fig. 3. The pressure profile in a journal bearing lubricated with a Newtonian fluid and with cavitation taken into account. The operating conditions are shown in Table 1. To match the dimensionless groups used in the figures from the references, the pressure is scaled with the cavitation pressure, $\bar{p}_{cav}$.

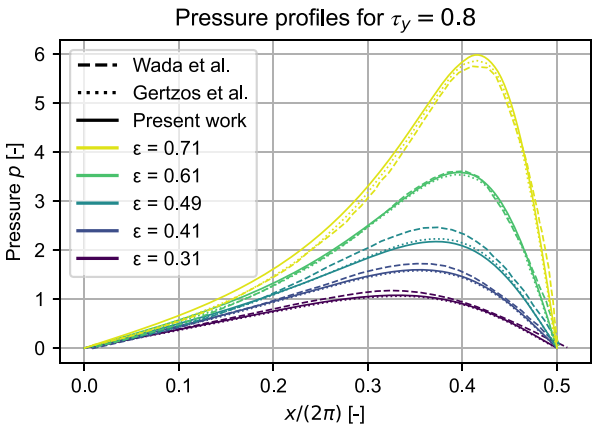

Fig. 4. The pressure profiles for several eccentricities in a journal bearing lubricated with a Bingham fluid with cavitation implemented with the half-Sommerfeld boundary condition. The operating conditions are shown in Table 1.

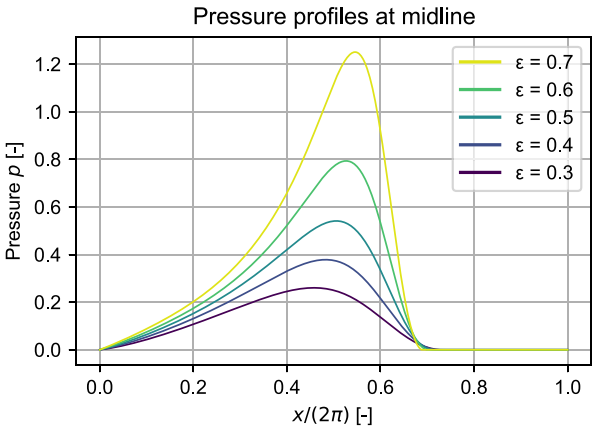

Fig. 5. The pressure profiles for several eccentricities in a journal bearing lubricated with a Herschel–Bulkley fluid with cavitation taken into account. The operating conditions are shown in Table 1.

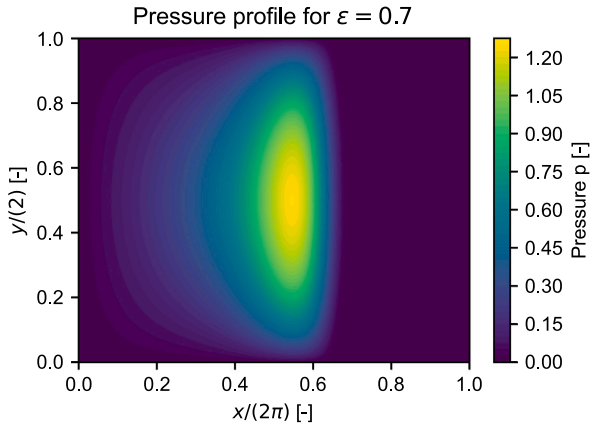

Fig. 6. The 2D pressure profile for an eccentricity of 0.7, as calculated for a journal bearing lubricated with a Herschel–Bulkley fluid with cavitation taken into account. The operating conditions are shown in Table 1.

$$W = \left(\left(\iint_S p \cos(x) \mathrm{d}A \right)^2 + \left(\iint_S p \sin(x) \mathrm{d}A \right)^2 \right)^{\frac{1}{2}} \tag{38}$$

The values in the table confirm that the differences between the variants are indeed small, though they are not zero. This can be explained by the limited accuracy of both the lookup tables, and of the numerical integration routine used in the numerical variant of the model. The accuracy of both could be increased to reduce these differences, but this would result in increasing storage sizes for the lookup tables, and increasingly long calculation times for the integration routine.

All results shown up to this point were calculated for a mesh size of $h_e = 0.01$, as was mentioned in Section 2.4. To check if the results produced with this mesh size are accurate, it is necessary to establish whether the models are mesh-convergent. This is done using the load capacity, by comparing the FEM results of both model variants with a good estimate of the exact result. This estimate is obtained with Aitken's extrapolation method (also known as Aitken's δ^2-process), which uses three successive values in a converging series to calculate an improved estimate of the first value [46]. With this method, the relative error between the FEM-calculated load capacity and the Aitken estimate can be determined as a function of the mesh size. This error can be found in Fig. 7, proving that the models are indeed mesh-convergent, and that the results are sufficiently accurate with a mesh size of 0.01.

The previous results have shown that the analytical and numerical variants produce effectively identical pressure profiles. The only comparison left is therefore to check whether the analytical variant is faster, as was claimed at the start of this paper. The required computational times for both variants can be found in Fig. 8 as a function of the mesh size and the number of degrees of freedom. This figure shows the time required to solve the test case from Table 1 for the five different eccentricity values from Table 2. It is easily seen that the analytical variant of the model is indeed faster than the numerical variant, with the computational time being reduced by about a factor 2, independent of mesh size.

This demonstrates that the approach used in this paper, where the flow factor integrals appearing in Dowson's generalised Reynolds equation were evaluated analytically for a Herschel–Bulkley fluid model, is an effective way of reducing the required computational time without losing any accuracy.

4. Conclusion

This paper presents a method for efficiently solving the pressure profile in a thin film flow of a non-Newtonian lubricant. Specifically,

Table 2
The relative differences in peak pressure and load capacity between the numerical and analytical variants of the model.

Eccentricity ϵ	0.3	0.4	0.5	0.6	0.7
Relative difference in peak pressures	1.55e−5	0.675e−5	0.118e−5	0.313e−5	0.113e−5
Relative difference in load capacity	3.268e−7	4.088e−7	1.200e−7	0.623e−7	1.290e−6

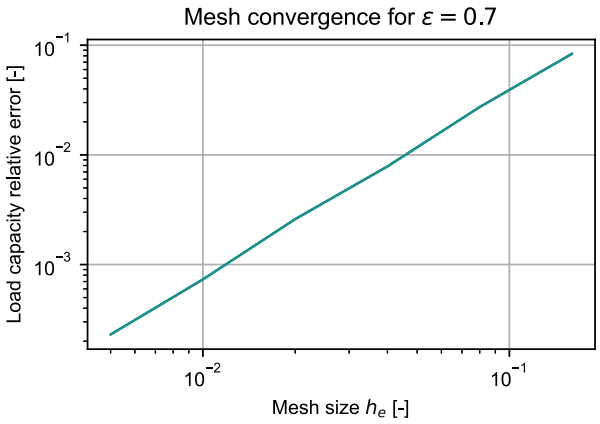

Fig. 7. The relative error between the FEM-calculated load capacity and an estimate of the exact load capacity, as a function of the mesh size for an eccentricity of $\epsilon = 0.7$. Only the line for the analytical variant of the model is shown.

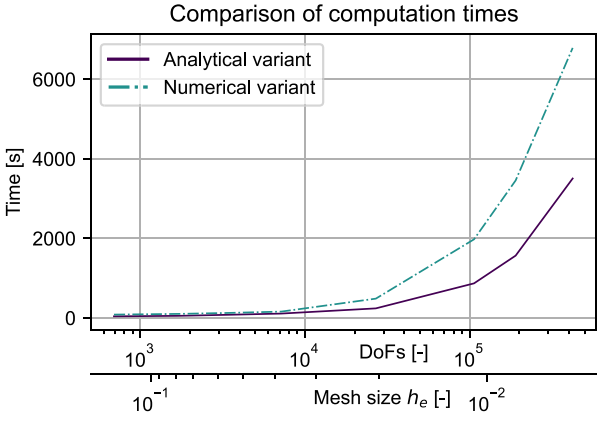

Fig. 8. The computational time required to solve the analytical and numerical variants of the model for five different eccentricities. The x-axis indicates the number of degrees of freedom, as well as the corresponding mesh size.

the 2D generalised Reynolds equation has been used to include shear-dependent viscosity effects, which were modelled with the Herschel–Bulkley model, allowing for both a yield stress as well as shear-thinning or shear-thickening effects. Similar studies exist in literature, however, those studies generally use computationally expensive numerical integration to evaluate several viscosity-dependent integrals that appear in the generalised Reynolds equation. Furthermore, the Herschel–Bulkley model is frequently regularised, to prevent convergence issues due to the discontinuity in the viscosity caused by the yield stress. It has been shown in this paper that these integrals can also be evaluated analytically, and without the use of regularisation. The resulting expressions depend on the so-called Appell F1 function, a well-defined but relatively obscure mathematical function. Due to a lack of fast and robust implementations of this function, pre-calculated lookup tables were used instead, which only have to be recalculated when the fluid properties are changed. The results produced by the final model (which includes mass-conserving cavitation) agree with literature, and show that the model produces effectively identical pressure profiles for both the numerically and analytically evaluated integrals without regularisation. The only difference being that the analytical variant does so about twice as fast, independent of mesh size. This decrease in computation time means that the model can be used more efficiently than the existing models, for example in design optimisation studies.

CRediT authorship contribution statement

G.H.G. van der Meer: Writing – original draft, Visualization, Validation, Software, Methodology. **R.A.J. van Ostayen:** Writing – review & editing, Supervision, Software, Methodology, Conceptualization.

Declaration of competing interest

The authors declare that they have no known competing financial interests or personal relationships that could have appeared to influence the work reported in this paper.

Acknowledgements

This research is funded and supported by TKI Maritiem and Bifröst Research and Development B.V. Bifröst Research and Development B.V. is a subsidiary of the AEGIR-Marine Group. AEGIR-Marine contact person: Dennis Nahuijsen - Manager Technology & Innovation.

Appendix. Derivation of the generalised Reynolds equation with cavitation

The cavitation algorithm used in this paper requires numerical stabilisation, otherwise the convection-dominated nature of the cavitated region will result in oscillations in the pressure solution. A simple and effective stabilisation technique is artificial diffusion (AD), which was used by Alakhramsing et al. to stabilise the standard Reynolds equation [32]. This paper follows their derivation, but applies it to the generalised Reynolds equation instead. Furthermore, isotropic diffusion will be used, with the diffusion coefficient for the x-direction (streamline) being applied to the y-direction (crosswind direction) as well. The amount of diffusion added to the crosswind direction will therefore be larger than necessary, but while the effect on the pressure solution was found to be minimal, convergence of the solver was much improved.

As was mentioned in the main text, a new variable ξ is used to model both the pressure p and the lubricant fraction ψ. The equations defining these relationships are repeated below.

$$p = (\xi \geq 0)\xi \tag{A.1}$$

$$\psi = 1 + (\xi < 0)c_f\xi \tag{A.2}$$

Using Eq. (A.1) to substitute for the pressure in the generalised Reynolds equation (Eqs. (10) and (11)) results in Eq. (A.3) in the x-direction. Here $u_{x,a}$ and $u_{x,b}$ are the x components of $\vec{u}_a$ and $\vec{u}_b$ respectively, and an artificial diffusion term k_{AD} is added to the cavitated region where $\xi < 0$.

$$\frac{\partial}{\partial x}\left(-\left(h^3\left(F_2 - \frac{F_1^2}{F_0}\right)(\xi \geq 0) + k_{AD}(\xi < 0)\right)\frac{\partial \xi}{\partial x} + \psi h\left(1 - \frac{F_1}{F_0}\right)u_{x,b} + \psi h\frac{F_1}{F_0}u_{x,a}\right) = 0 \tag{A.3}$$

The remainder of this derivation will focus on finding an optimal value for k_{AD} such that all oscillations are suppressed, without the

introduction of excessive damping. The coefficient k_{AD} will be defined by Eq. (A.4).

$$k_{AD} = h_e u_{AD} \tag{A.4}$$

Here h_e is the typical size of the mesh elements, and u_{AD} the convection coefficient from Eq. (A.3). This term is defined by Eq. (A.5), where c_f is a transformation constant and c_{AD} is given by Eq. (A.6).

$$u_{AD} = hc_{AD}\,(\xi < 0)\,c_f \tag{A.5}$$

$$c_{AD} = \left(1 - \frac{F_1}{F_0}\right)u_{x,b} + \frac{F_1}{F_0}u_{x,a} \tag{A.6}$$

Eq. (A.3) could now be solved by tweaking the amount of cavitation using c_f. However, it is known that the oscillations in the pressure solution will be the largest in the cavitated region near the reformation boundary. The minimal value for c_f should therefore be determined on this boundary. One way of doing this is to equate the flow rates at the reformation boundary as calculated in both the cavitated and full film regions ($q_{x,cav}$ and $q_{x,full}$ respectively, see Eq. (A.7)). Substituting for $q_{x,cav}$ and $q_{x,full}$ results in Eq. (A.8), where it should be noted that $\xi \geq 0$ and $\psi = 1$ in the full film region.

$$q_{x,cav} = q_{x,full} \tag{A.7}$$

$$hc_{AD}\psi = -h^3\left(F_2 - \frac{F_1^2}{F_0}\right)\frac{\partial \xi}{\partial x} + hc_{AD} \tag{A.8}$$

One method for solving this equation is to expand the derivatives using numerical differences, as shown in Eq. (A.9). Here ξ_r is defined at point r in the cavitated region close to the reformation boundary, and ξ_{r+1} is defined at the neighbouring downstream point $r+1$ which lies in the full film region close to the boundary.

$$hc_{AD}(1 + c_f\xi_r) = -h^3\left(F_2 - \frac{F_1^2}{F_0}\right)\frac{\xi_{r+1} - \xi_r}{h_e} + hc_{AD} \tag{A.9}$$

Solving Eq. (A.9) for c_f results in Eq. (A.10). Since $\xi_{r+1} \geq 0$ in the full film region and $\xi_r < 0$ in the cavitated region, the minimum value of c_f that is required for numerical stability is given by Eq. (A.11).

$$c_f = \left(F_2 - \frac{F_1^2}{F_0}\right)\frac{h^2\left(1 - \frac{\xi_{r+1}}{\xi_r}\right)}{h_e c_{AD}} \tag{A.10}$$

$$c_f \geq \left(F_2 - \frac{F_1^2}{F_0}\right)\frac{h^2}{h_e c_{AD}} \tag{A.11}$$

This minimum value for c_f can now be applied to Eq. (A.3), using Eqs. (A.4) and (A.5). Finally, repeating this process for the y-direction (crosswind direction) will results in Eq. (14). Note that the boolean terms that were still present in Eq. (A.3) have dropped out due to this choice of c_f.

Data availability

Data will be made available on request.

References

[1] Gecim BA. Non-Newtonian effects of multigrade oils on journal bearing performance. Tribol Trans 1990;33(3):384–94. http://dx.doi.org/10.1080/10402009008981968, publisher: Taylor & Francis.

[2] Khonsari MM, Booser ER. Applied tribology : bearing design and lubrication. Hoboken, NJ: John Wiley & Sons Inc.; 2017.

[3] Michalec M, Svoboda P, Krupka I, Hartl M. Tribological behaviour of smart fluids influenced by magnetic and electric field – A review. Tribol Ind 2018;40(4):515–28. http://dx.doi.org/10.24874/ti.2018.40.04.01, publisher: Faculty of Engineering, University of Kragujevac.

[4] Milne AA. A theory of rheodynamic lubrication lubrication and wear division: Lubrication and wear division. Kolloid-Z 1954;139(1–2):96–101. http://dx.doi.org/10.1007/BF01502330.

[5] Pinkus O, Sternlicht B. Theory of hydrodynamic lubrication. McGraw-Hill; 1961.

[6] Ghaffari A, Hashemabadi SH, Ashtiani M. A review on the simulation and modeling of magnetorheological fluids. J Intell Mater Syst Struct 2015;26(8):881–904. http://dx.doi.org/10.1177/1045389X14546650.

[7] de Vicente J, Klingenberg DJ, Hidalgo-Alvarez R. Magnetorheological fluids: A review. Soft Matter 2011;7(8):3701–10. http://dx.doi.org/10.1039/c0sm01221a.

[8] Bird RB, Dai GC, Yarusso BJ. The rheology and flow of viscoplastic materials. Rev Chem Eng 1983;1(1):1–70. http://dx.doi.org/10.1515/revce-1983-0102.

[9] Bird RB. Dynamics of polymeric liquids, volume 1: fluid mechanics. Wiley; 1987.

[10] Dang RK, Goyal D, Chauhan A, Dhami SS. Effect of non-newtonian lubricants on static and dynamic characteristics of journal bearings. Mater Today: Proc 2020;28:1345–9. http://dx.doi.org/10.1016/j.matpr.2020.04.727.

[11] Bouyahia F, Hajjam M, El Khlifi M, Souchet D. Three-dimensional non-Newtonian lubricants flows in sector-shaped, tilting-pads thrust bearings. Proc Inst Mech Eng J 2006;220(4):375–84. http://dx.doi.org/10.1243/13506501JET92, publisher: Professional Engineering Publishing.

[12] Kauzlarich JJ, Greenwood JA. Elastohydrodynamic lubrication with Herschel-Bulkley model greases. A S L E Trans 1972;15(4):269–77. http://dx.doi.org/10.1080/05698197208981427.

[13] Wang X, Li H, Li M, Bai H, Meng G, Zhang H. Dynamic characteristics of magnetorheological fluid lubricated journal bearing and its application to rotor vibration control. J Vibroeng 2015;17(4):1912–28, number: 4 Publisher: JVE International Ltd. URL https://www.extrica.com/article/15935.

[14] Wada S, Hayashi H, Haga K. Behavior of a Bingham solid in hydrodynamic lubrication - 1. general theory. Bull JSME 1973;16(92):422–31. http://dx.doi.org/10.1299/kikai1938.38.1617.

[15] Wada S, Hayashi H, Haga K. Behavior of a Bingham solid in hydrodynamic lubrication - 2. application to step bearing. Bull JSME 1973;16(92):432–40. http://dx.doi.org/10.1299/kikai1938.38.1627.

[16] Wada S, Hayashi H, Haga K. Behavior of a Bingham solid in hydrodynamic lubrication : Part 3, application to journal bearing. Bull JSME 1974;17(111):1182–91. http://dx.doi.org/10.1299/jsme1958.17.1182.

[17] Tichy JA. Hydrodynamic lubrication theory for the Bingham plastic flow model. J Rheol 1991;35(4):477–96. http://dx.doi.org/10.1122/1.550231.

[18] Dowson D. A generalized Reynolds equation for fluid-film lubrication. Int J Mech Sci 1962;4(2):159–70. http://dx.doi.org/10.1016/S0020-7403(62)80038-1.

[19] Dorier C, Tichy J. Behavior of a Bingham-like in lubrication flows. J Non-Newton Fluid Mech 1992;45(3):291–310. http://dx.doi.org/10.1016/0377-0257(92)80065-6.

[20] Khlifi ME, Souchet D, Hajjam M, Bouyahia F. Numerical modeling of non-Newtonian fluids in slider bearings and channel thermohydrodynamic flow. J Tribol 2007;129(July):695–9. http://dx.doi.org/10.1115/1.2736732.

[21] Kim JH, Seireg AA. Thermohydrodynamic lubrication analysis incorporating Bingham rheological model. J Tribol 1998;122(1):137–46. http://dx.doi.org/10.1115/1.555336.

[22] Sahu K, Sharma SC. A simulation study on the behavior of magnetorheological fluid on Herringbone-grooved hybrid slot-entry bearing. Tribol Trans 2019;62(6):1099–118. http://dx.doi.org/10.1080/10402004.2019.1649775, publisher: Taylor and Francis Inc.

[23] Sharma SC, Yadav SK. Performance analysis of a fully textured hybrid circular thrust pad bearing system operating with non-Newtonian lubricant. Tribol Int 2014;77:50–64. http://dx.doi.org/10.1016/j.triboint.2014.04.013.

[24] Sharma SC, Khatri CB. Electro-rheological fluid lubricated textured multi-lobe hole-entry hybrid journal bearing system. J Intell Mater Syst Struct 2018;29(8):1600–19. http://dx.doi.org/10.1177/1045389X17742731.

[25] Frigaard IA, Nouar C. On the usage of viscosity regularisation methods for visco-plastic fluid flow computation. J Non-Newton Fluid Mech 2005;127(1):1–26. http://dx.doi.org/10.1016/j.jnnfm.2005.01.003.

[26] Lampaert SGE, van Ostayen RAJ. Lubrication theory for Bingham plastics. Tribol Int 2020;147:106160. http://dx.doi.org/10.1016/j.triboint.2020.106160.

[27] Bompos DA, Nikolakopoulos PG. CFD simulation of magnetorheological fluid journal bearings. Simul Model Pract Theory 2011;19(4):1035–60. http://dx.doi.org/10.1016/j.simpat.2011.01.001, publisher: Elsevier B.V..

[28] Gertzos KP, Nikolakopoulos PG, Papadopoulos CA. CFD analysis of journal bearing hydrodynamic lubrication by Bingham lubricant. Tribol Int 2008;41(12):1190–204. http://dx.doi.org/10.1016/j.triboint.2008.03.002.

[29] Urreta H, Aguirre G. Hydrostatic journal bearing and pressurized seals for machine tool spindles based on active magnetic fluids: magnetorheological fluids and ferrofluids. In: Proceedings of the 18th international conference of the European Society for Precision Engineering and Nanotechnology. 2018, p. 530, URL https://www.euspen.eu/knowledge-base/ICE18278.pdf.

[30] COMSOL AB. Comsol multiphysics® version 6.1. 1986-2023, https://www.comsol.com/.

[31] Shukla JB, Kumar S, Chandra P. Generalized reynolds equation with slip at bearing surfaces: Multiple-layer lubrication theory. Wear 1980;60(2):253–68. http://dx.doi.org/10.1016/0043-1648(80)90226-4.

[32] Alakhramsing S, van Ostayen R, Eling R. Thermo-hydrodynamic analysis of a plain journal bearing on the basis of a new mass conserving cavitation algorithm. Lubricants 2015;3(2):256–80. http://dx.doi.org/10.3390/lubricants3020256.
[33] Wolfram Research, Inc. Mathematica, version 13.3. 2023, https://www.wolfram.com/mathematica/.
[34] Olver FW, Lozier DW, Boisvert R, Clark CW. The NIST handbook of mathematical functions. NIST; 2010, URL https://www.nist.gov/publications/nist-handbook-mathematical-functions.
[35] Cabral-Rosetti LG, Sanchis-Lozano MA. Generalized hypergeometric functions and the evaluation of scalar one-loop integrals in Feynman diagrams. 1998, http://dx.doi.org/10.48550/arXiv.hep-ph/9809213.
[36] Barber MN, Ninham BW. Random and restricted walks: theory and applications. Mathematics and its applications, vol. 10, New York: Gordon and Breach; 1970.
[37] Colavecchia FD, Gasaneo G. f1: a code to compute Appell's $f1$ hypergeometric function. Comput Phys Comm 2004;157(1):32–8. http://dx.doi.org/10.1016/S0010-4655(03)00490-9.
[38] Bailey WN. Generalized hypergeometric series. Cambridge tracts in mathematics and mathematical physics, no. 32, London: Cambridge University Press; 1893, 1935.
[39] Weisstein EW. Appell hypergeometric function. From MathWorld—A Wolfram Web Resource. 2024, https://mathworld.wolfram.com/AppellHypergeometricFunction.html, retrieved on 22-04-2024.
[40] The MathWorks Inc. Matlab version: 9.11.0 (r2021b). 2021, https://www.mathworks.com.
[41] Arcadia C. Bivariate appel hypergeometric function of the first kind. 2017, https://www.mathworks.com/matlabcentral/fileexchange/61066-bivariate-appel-hypergeometric-function-of-the-first-kind, retrieved on 29-04-2024.
[42] van der Meer GHG. Appell f1 hypergeometric function. 2024, https://nl.mathworks.com/matlabcentral/fileexchange/174390-appell-f1-hypergeometric-function, retrieved on 24-10-2024.
[43] Brewe DE. Theoretical modeling of the vapor cavitation in dynamically loaded journal bearings. J Tribol 1986;108(4):628–37. http://dx.doi.org/10.1115/1.3261288.
[44] Elrod HG. A cavitation algorithm. J Lubr Technol 1981;103(3):350–4. http://dx.doi.org/10.1115/1.3251669.
[45] Jakobsson B, Floberg L. The finite Journal bearing, considering vaporization, Chalmers tekniska högskola. Göteborg: Gumperts Förlag; 1957, oCLC: 718857301.
[46] Abramowitz M, Stegun IA, United States National Bureau of Standards. Handbook of mathematical functions with formulas, graphs, and mathematical tables. Applied mathematics series, no. 55, Washington, D.C.: National Bureau of Standards; 1964.